V- and *W*-Band Millimeter-Wave GaN MMICs

TIMOTHY SONNENBERG (Student Member, IEEE), **ANTHONY ROMANO** (Student Member, IEEE),
SHANE VERPLOEGH (Member, IEEE), MAURICIO PINTO (Member, IEEE), **AND ZOYA POPOVIĆ (Fellow, IEEE)**

(Invited Paper)

Department of Electrical, Computer, and Energy Engineering, University of Colorado Boulder, Boulder, CO 80309 USA

CORRESPONDING AUTHOR: Timothy Sonnenberg (e-mail: Timothy.Sonnenberg@colorado.edu).

ABSTRACT   This paper gives an overview of published results with GaN MMICs for millimeter-wave front ends at frequencies above 60 GHz, including power and low-noise amplifiers, switches, phase shifters, frequency multipliers and oscillators. Some design methods and demonstrated experimental results obtained at W band from MMICs fabricated in a 40-nm GaN on 50–μm SiC process are then presented. These include 75 to 110 GHz power amplifiers with 20–27 dBm output power and 10–17 dB gain, switches with 2 dB insertion loss and 20 dB isolation, and continuous phase shifters with 2–11 dB loss and 0°–90° of tunable phase shift. Additional MMICs include frequency doublers and triplers, oscillators, circulators and mixers, designed for higher levels of on-chip integration towards a W-band front end.

INDEX TERMS   Broadband, frequency doubler, front end, GaN, MMIC, millimeter wave, MTT 70th Anniversary Special Issue, phase shifter, power combining, power amplifier, stability, switch, V-band, W-band.

I. INTRODUCTION

The millimeter-wave part of the electromagnetic spectrum above 50 GHz, in V (50–75 GHz) and W bands (75–110 GHz), is currently used for backhaul communication links for earth and space systems, imaging, spectroscopy, radioastronomy, and automotive radar. This frequency range offers high-data throughput from modest fractional bandwidth, high imaging resolution resulting from short wavelengths, and lower wave attenuation in atmospheric window frequency bands, as well as when propagating through dust, smoke and fog [1], [2]. The frequency allocations in V and W bands are still evolving. This paper presents an overview of state-of-the-art front-end gallium nitride (GaN) integrated circuits, Fig. 1, needed for communications, sensing, imaging, medical and industrial applications, overviewed briefly below.

With growing user demand for extensive multimedia content, communication links are under development at Ka-band and looking towards higher frequencies such as the unlicensed allocations at V-band in the 57–64 GHz and 64–71 GHz bands [3], [4], the 60 GHz WiFi IEEE bands, and the FCC private sector point-to-point links from 71–76, 81–86, and 92–95 GHz. Demonstrated high data rate communication systems operating at 92 GHz and achieving 6.5 Gbps with quadrature

amplitude modulation (128-QAM) are shown with GaN front-ends [5], and data rates up to 8 Gbps with 16-QAM signals are shown in a 6 m range at 75 GHz wireless link using 100-nm InGaAs mHEMT technology for the LNA and mixer [6]. Additionally, millimeter-wave communications are attractive for fixed satellite services and space exploration missions [7]. In already developed high throughput geostationary multimedia services at K-band, W-band carrier frequencies could reduce the number of pathways for data transmission allowing allocated resources to reroute during failures.

High resolution imaging with W-band phased array systems is accomplished as a result of the small wavelengths [8], [9]. Developed imaging systems function as radars where the point scatterers can be resolved within 1–2 cm accuracy. Security screening for weapon detection is currently used at Ka-band frequencies, but also at 92 GHz, e.g. [10]. Imaging and gesture detection has been shown commercially from a Google Soli device at 60 GHz [11] and is being developed at 94 GHz [12]. Various radar platforms have been demonstrated such as a 3-D imaging 100-GHz multiple input multiple-output (MIMO) frequency-modulated continuous-wave (FMCW) radar in [13] and a 93.5–94.5 GHz MIMO FMCW radar in [14]. Hidden object detection and identification has been
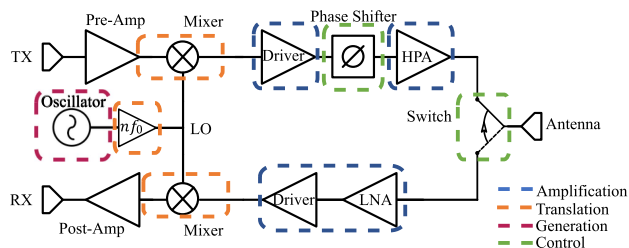
FIGURE 1. Simplified analog front end of a millimeter-wave system, showing individual MMIC components and their respective functional roles.
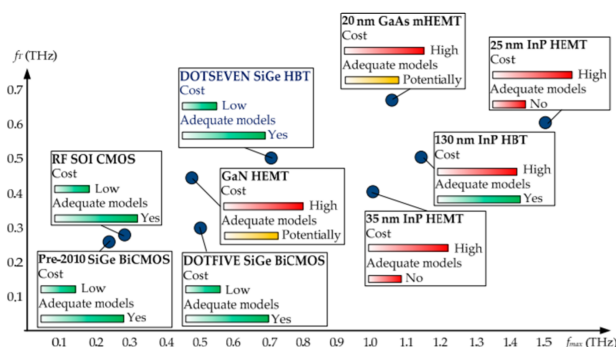

FIGURE 2. Comparison of semiconductor processes for scaled frequency performance, as a function of transition frequency over maximal frequency. (Reproduced from [28].).

demonstrated through walls and various materials in [15], [16], [17]. The automotive radar 76–77 and 77–81 GHz bands satisfy the imaging resolution and data speed requirements for automated driving [18]. Multiple low-power W-band phased arrays using silicon technology were demonstrated for automotive radar, e.g. [19], [20].

There are a number of new applications under development at W-band, e.g. industrial vibrometry [21], and CW radar are shown for measuring human respiration and heartbeat [22], while other medical applications include imaging of burns [23], and in biology research W-band radar was used to detect insect wing-beat frequency for observing migrations [24].

High attenuation of the atmosphere and lack of devices that can generate the required power results in limited use of the higher part of the millimeter-wave spectrum. Solid-state power amplifiers (PAs) are limited in total output power, bandwidth, and efficiency, and are expensive due to the need for power combining and low-loss packaging of the analog front end. Although silicon-based circuits have shown high-frequency operation with medium level power from power-combined devices, for watt-level power, III-V semiconductors are needed. High-performing 0.1-μm gate length pseudomorphic InGaAs high electron mobility transistors (HEMT) processes developed in the 1980s [25] allowed a path for millimeter-wave solid-state systems operating at W-band with various front-end MMIC circuits. Innovative techniques in spatial power combining were introduced using GaAs technology, where traditional binary corporate combining became limited by loss. For example, at 61 GHz, a 16×17 lens array using a total of 272 GaAs MMICs achieved a total of 36 W [26]. These developments quickly found their place in commercial and defense industry ranging from airborne and ground-based radars, satellite communications, to missile terminal guidance phase decoys, many of which still remain GaAs-based systems due to the robustness offered by the technology. With research at the turn of the century bringing wide band-gap semiconductors to the stage, gallium-nitride (GaN) has been improving high-frequency performance with operating frequencies in the hundreds of GHz [27], [28]. Fig. 2 shows a useful qualitative comparison of different semiconductor technologies as a function of f_T and f_{max} up to 1.5 THz.

A number of recent millimeter-wave GaN processes with gate lengths in the 20–90 nm range have shown high performance across V and W bands [29], [30], [31], [32]. In this paper, we give an overview of published results for various GaN MMICs at frequencies above 50 GHz, followed by a more detailed description of various current W-band front-end MMIC designs in the HRL 40-nm technology. Section II reviews published power amplifier GaN MMICs, followed by GaN control circuits such as switches and phase shifters, as well as frequency generation and translation MMICs. Section III describes the design process for three W-band GaN MMIC PAs with on-chip power combining. Sections IV and V focus on control circuits, with switches and continuous phase shifter MMIC design and measurements. Section VI gives a brief overview of an oscillator circuit and several frequency multipliers. Finally, Section VII gives some additional W-band MMIC examples and points to future directions.

II. REVIEW OF V- AND W- BAND STATE-OF-THE-ART GAN MMICS

Various GaN processes on either SiC or Si substrates currently achieve cutoff frequencies above 150 GHz. While SiC as a substrate offers better thermal properties, Si offers lower cost and potential of integration with other electronics. As examples, an f_T up to 275 GHz is shown in a 40-nm GaN on SiC HEMT process [30], and $f_T = 170$ GHz in a GaN on Si process in [32]. Breakdown voltages beyond 20 V while operating in the hundreds of GHz range allow these device to achieve high output powers [27]. Power densities as high as 3 W/mm are shown at W-band in GaN on SiC [30], and 2.5 W/mm with 8.5 dB of gain at 94 GHz with a 10 V supply voltage in a 40-nm GaN on Si process [32]. Device efficiency is also increasing at W band, with 45% PAE reported for a 3 W/mm high power device at 94 GHz, while the same device can reach 56% PAE with an output power density of 780 mW/mm [30]. Advanced GaN processes also present minimum noise figures below 2 dB in V and W bands for low noise designs in 40 nm and 90 nm GaN on SiC processes [29], [30]. The ability to design with multiple gate lengths allows

TABLE 1. Comparison of Narrow-Band *V*- and *W*-Band GaN HEMT Amplifiers

Freq (GHz)	Frac. BW (%)	P_{out} (dBm)	PAE (%)	Gain (dB)	Year Ref.
71-76	6.8%	34.9	27.8%	15.2	2012 [36]
71-86	19.1%	31.4	9.9%	25.8	2018 [37]
84-95	12.3%	29.2	14.7%	19.6	2010 [38]
90-92	2.2%	32.3	11%	15	2011 [39]
77.8-89	13.4%	31	12.3%	17	2016 [40]
86–94	8.8%	30.6	8%	12	2017 [41]
88-93	5.5%	34	14%	15	2017 [42]
90-97	7.5%	37.8	18.3%	15	2020 [43]

TABLE 2. Comparison of Broad-Band *V*- and *W*-Band GaN HEMT Amplifiers

Freq (GHz)	Frac. BW (%)	P_{out} (dBm)	PAE (%)	Gain (dB)	Year Ref.
6-52	158.6%	28	20%	8-12	2020 [44]
70-105	40%	24.5	6%	16	2012 [45]
80-100	22.2%	35	-	8	2013 [46]
75-100	28.6%	33	-	15	2016 [47]
70-110	44.4%	28.6	6.5%	12	2018 [48]
71-110	43.3%	24.2	6.5%	10	2021 [49]
75-110	**37.8%**	**20**	**8 %**	**11**	**[50]***
75-110	**37.8%**	**25**	**9.6 %**	**15**	**[50]+**
75-110	**37.8%**	**27**	**3 %**	**23**	**This work'**

* Unit-B Amplifier - @ P_{IN} = 9 dBm and 86 GHz
+ Balanced - @ P_{IN} = 10 dBm and 76 GHz
' Driver + Serial - @ P_{IN} = 4 dBm and 90 GHz

for increased complexity, such as low noise/high gain stages followed by high linearity stages in a single LNA [33].

A. V- AND W-BAND GAN MMIC PAS

The general challenges for W-band high-power solid-state transmitters are achieving high output power (ERP) in a small footprint and with reasonable efficiency. Ultra-high power vacuum tubes have been demonstrated to generate several hundreds of kW at W-band, e.g. [34], but suffer from narrow bandwidth and require large high-voltage power supplies and magnets to operate. The wide bandgap of GaN and high associated operating voltages make it the semiconductor of choice for high-power solid-state transmitters. The SiC substrate additionally offers good thermal properties compared to GaAs and Si. The highest published solid-state W-band transmitter produces around 6.8 kW and is intended for an active denial weapon [35]. The transmitter spatially coherently combines 8,192 GaN-on-SiC MMIC PAs, each with over 1 W of power and PAE > 20% around 93 GHz. This approach is modular and therefore scalable, with high demonstrated power-combining efficiency.

Various GaN power amplifiers at V and W bands have been demonstrated. State-of-the-art published results are summarized in Tables 1 and 2 for narrowband and broadband performance, respectively. Power levels as high as 37 dBm with 18.3% efficiency are reported for a power-combined amplifier over a narrow 7% bandwidth at 95 GHz in a 100-nm process [43]. On the other hand, a 44% bandwidth from 70–110 GHz with 26 dBm peak power and a gain of 16±2 dB is shown in [48]. Broadband amplifier design is challenging because of stability and the fundamentally lower efficiency, output power and gain compared to narrowband designs. Fig. 3 shows a summary plot of achieved measured output power over frequency across W band, with photos of the MMIC PAs. Broadband power combining of watt-level MMICs to achieve 37 W from 75–100 GHz is shown in [51].

B. V- AND W-BAND GAN LOW-NOISE AMPLIFIERS

The wide bandgap and operating voltages of GaN HEMTs make them attractive for power amplification, while the noise
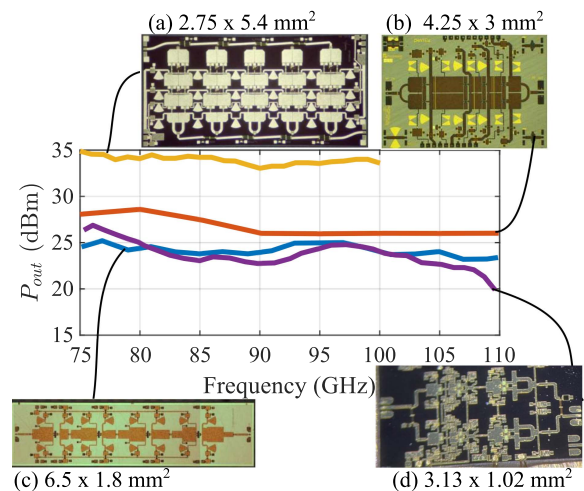

FIGURE 3. State-of-the-art published broadband W-band power amplifiers output power over frequency showing: (a) five serially combined 3-stage unit PAs made in 150 nm GaN on 50 μm SiC [52]; (b) 4-stage power combined 100 nm GaN on 75 μm SiC [48]; (c) 4-stage 100 nm GaN PA [49]; and (d) 3-stage balanced 40 nm GaN on 50 μm SiC PA [50].

performance of GaN low-noise amplifiers (LNAs) display competitive noise figures with other technologies. Additionally, these technologies come with the comparative advantage of high linearity and high power handling. Table 3 summarizes state-of-the-art published GaN MMICs operating within V and W bands (50–110 GHz). The lowest noise figure of 1.8–2.4 dB is reported in the wideband four-stage design of [53] using the advanced 40 nm T-gate device process, the lowest gate width of all reported GaN LNAs. Another wideband five-stage LNA is also reported in this paper. Furthermore, a five-stage balanced LNA in the same process is presented in [54] with similar bandwidth and gain as in [53], but with greater linearity over input power and less overall power consumption. A four-stage LNA is published in [55] using a 70 nm gate process which reports low noise figure between 2.8 and 3.3 dB.

TABLE 3. Comparison of *V*- and *W*-Band GaN LNAs

Freq (GHz)	Gain (dB)	NF (dB)	P_{1dB} (dBm)	P_{DC} (mW)	Year Ref.
75-110	20-30	1.8-2.4*	11-13	176	2014 [53]
65-110	> 25	2.3-3.2*	14	418	2014 [53]
60-105	23-24.5	< 4	20	225	2017 [54]
63-101	21-24	2.8-3.3	−16 − −10	307	2022 [55]
75-83	15.5-16.1	3.5-4.2	-	200	2021 [56]
91-96	18-19.1	3.3-3.8	-	200	2021 [56]
86-98	20	3.5	-	128	2016 [57]
82-86	25	5.6	15	800	2011 [58]
106.5-113.5	30	7.6	15.5	2400	2018 [59]
77.8-84	17.5-20.5	3.8-4.7	8.5-12	190	2020 [60]

* Simulated

TABLE 4. State of the Art *V*- and *W*-Band GaN Oscillators

Center Freq (GHz)	Tuning Range (%)	Phase Noise (dBc/Hz)	P_{out} (dBm)	P_{DC} (W)	Ref.
53	2.3	-97 at 1 MHz offset	11	4.8	[62]
67	4.9	-83 at 1 MHz offset	19.5	0.66	[63]
70.75	2.1	-65.2 at 1 MHz offset	19.28	1.47	[64]
84	1.2	-120 at 10 MHz offset	-0.67	0.34	[65]
89.2	8	-90.2 at 1 MHz offset	10.6	0.65	[66]
82	11	-106.4 at 10 MHz offset	22.6	1.08	[67]
89	3.3	-110.6 at 10 MHz offset	22.5	1.2	[67]

As the device gate lengths increase and the transistors operate towards their upper frequency limit, reported noise figure trends upward and bandwidth decreases. The dual band design in [56] operates with noise figures of 3.5–4.2 dB and 3.3–3.8 dB for the respective 75–83 GHz and 91–96 GHz bands. The remaining circuits [57], [58], [59], [60] are designed in 100 nm GaN processes. The LNA in [59] is noteworthy for having the highest gain of all the tabulated millimeter wave GaN LNAs, and being the only cascode design, which takes additional stability considerations. Finally, [60] reports the only GaN on silicon substrate LNA with the goal of providing a lower cost circuit, but at the expense of its thermal properties compared to SiC. With the promising noise performance demonstrated to date, challenges remain in noise characterization at higher frequencies and lower noise figures.

C. CONTROL, FREQUENCY GENERATION AND TRANSLATION *V*- AND *W*-BAND GAN MMICS

Isolating the transmit and receive path of a transceiver is an essential function for front ends. Active circulators are a promising alternative to ferrite devices and provide the potential for gain in the transmit and receive paths of full-duplex front ends. These have been demonstrated across X-band in a GaAs MMIC [61], showing a path for W-band GaN implementation with an example currently in development shown in the last section. For half-duplex operation, switches have been developed and are reviewed in more detail in Section IV, with insertion loss on the order of 1–2 dB across W band in 100 nm [31] and 40-nm [53] GaN processes.

For fully integrated W-band transceivers, it remains a question whether the best approach is to generate signals directly at W-band, or to do so at lower frequencies and multiply the signal to the band of operation. We first review the state-of-the-art V- and W-band oscillator GaN MMICs. The frequency multiplication approach is shown in the block diagram of Fig. 1 and frequency multipliers are reviewed in Section VI along with some new results in a 40-nm process.

Table 4 summarizes demonstrated GaN MMIC oscillators. A standard method to design a microwave oscillator is with an unstable HEMT in the common source configuration with a resonator in the feedback path that determines the oscillation frequency and phase noise. The oscillators in [63], [64], [66], [67] realize this feedback by including a transmission line between the source terminal of the device and ground. Frequency tuning is performed by adjusting the reactance looking into the gate. An output buffer can isolate the oscillator core from impedance variations, while its bias can be adjusted to change the capacitive loading on the drain and tune the oscillation frequency [64], [67]. Varactors or diode connected devices with tunable gate bias have been shown to achieve a wider tuning range when connected at the gate of the oscillator core [63], [66], [67]. These oscillator topologies can operate at high frequencies with moderate phase noise performance and higher output power compared to other methods. A push-push VCO is implemented in [62] with two capacitively coupled common-gate configured devices. This oscillator operates at a lower frequency and requires more dc power than the common source designs, but was designed in a 200 nm process, while the rest use 120 nm or smaller gates. Finally, a balanced Colpitts oscillator was designed in [65] which exploits the resonance of an *LC* tank for its frequency generation. While this design quotes the smallest phase noise of all the circuits, it produces far less output power.

Following this brief review of the state-of-the-art in GaN MMICs at frequencies from 50–110 GHz, the design of several high-performing GaN MMICs in the 40-nm HRL T3 process is showcased with a goal of discussing possibilities and limitations of GaN technology for broadband circuits that cover W-band.

III. EXAMPLE W-BAND GAN PAS IN A 40-NM MMIC PROCESS

All designs are fabricated in the HRL T3 process featuring 40-nm GaN T-gates with f_T/f_{max} of 200/400 GHz and a
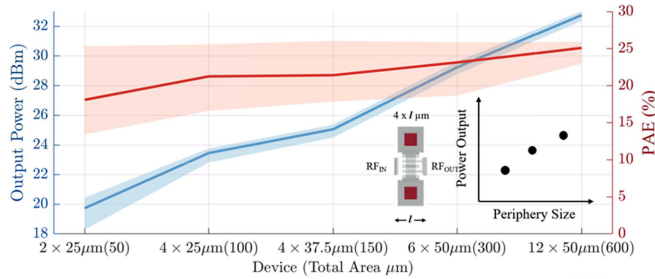
FIGURE 4. Plot of the maximum power output and corresponding efficiency with optimal impedances presented to the device input (match below −10 dB) and output (obtained by load-pull). The shaded area presents behavior across frequency from 75 to 110 GHz for each validated HEMT model, and for an extrapolated 4×25 μm HEMT model. All devices are biased at V_{DD}=12 V and $V_{GG} = -0.2$ V, and the compressed gain is in the range of 3–4 dB.
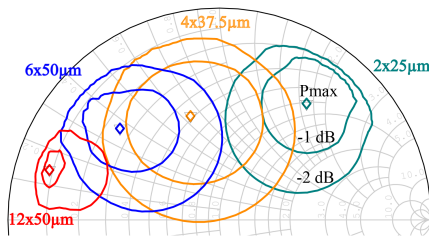

FIGURE 5. Loadpull impedance of the maximum power output and contours of −1 dB, −2 dB from the maximum. Optimal impedances are presented to the device input (match below −10 dB) and output (obtained by load-pull). The loadpull is shown at a frequency of 92 GHz for each validated HEMT model. All devices are biased at V_{DD}=12 V and $V_{GG} = -0.2$ V.

FIGURE 6. Surface current amplitude for 3-dB Lange couplers, with top showing a manifold with four right angle feeds common in balanced amplifiers, and bottom showing manifold with two straight and two right angle feeds used in serial combiners. The size of the balanced combiner is 590 × 1100 μm and the serial combiner is 585 × 2070 μm.

A. AMPLIFIER DESIGN AND SCALING

The low HEMT gain implies multiple stages for a useful PA, and power combining for useful output power. Four of the aforementioned HEMT models are used in a 3-stage PA design, where the last stage is reactively power combined. The staging ratio is determined based on interstage matching, as discussed in [50]. The broadband matching networks of the 3-stage PA consist of low-impedance transmission lines and stubs broadband matching, avoiding the use of capacitors as they are more prone to process variation than metal layers. Parallelizing the individual HEMTs with internally shared vias reduces the distance between transistors and allows a more compact circuit layout. dc blocking, stability and biasing is done through SiN capacitors and TaN resistors.

Minimizing the 3-stage PA footprint and designing the input and output ports of the 3-stage "unit" PA to be 50 Ω allows power combining at the circuit level. To further increase output power, two and three of such "unit" 3-stage PAs are combined on-chip in a balanced and serial [52] amplifier topology. To cover the entire 75–110 GHz range, Lange couplers may be used. A closer analysis of the Lange coupler for the serial combining architecture shows that current crowding at millimeter-wave frequencies affects circuit behavior. The coupling factor differs for different port transmission-line feeds of a Lange coupler, requiring an adjustment in distance between the coupled microstrip sections.

Fig. 6 shows the current distributions for two Lange couplers fed with 4-angled bends, used in balanced amplifier layout, and two-angled bends used for serial combiners layout. The full-wave simulated surface current magnitude for the coupled lines shows accumulation on the inside of the

breakdown voltage of >40 V on a 50 μm SiC substrate [27]. Device-level combining within a MMIC amplifier is done first, by scaling the device and choosing appropriate staging ratios, and then on-chip reactive or isolated combining. To determine the staging ratio and limits of possible power-added efficiency (PAE) and output power, harmonic balance simulations for non-linear Angelov HEMT models are performed. Shown in Fig. 4 is the range of maximum output power and corresponding PAE of 4×37.5 μm, 2×25 μm, 6×50 μm, and 12×50 μm HEMTs, validated at drain voltages of +2 V, +6 V, and +12 V. The associated output power load-pull contours for validated device sizes is shown in Fig. 5. In Figs. 4, 5 only the +12 V drain voltage at a quiescent drain current density of 150 mA/mm is considered. The input of each device is matched to better than −10 dB. The shaded area presents behavior across frequency from 75 to 110 GHz for each validated HEMT model. Note that the 4×25 μm device is the an extracted model, which adds uncertainty to the simulation. The best achievable power ranges between 24.5 and 25 dBm for the 4×37.5 μm device, with an efficiency variation from 18% to 28% across the band. All devices are biased at (V_{DD}=12 V, $V_{GG}= -0.2$ V), and the respective gain obtained from the HEMT models ranges from 3–4 dB.
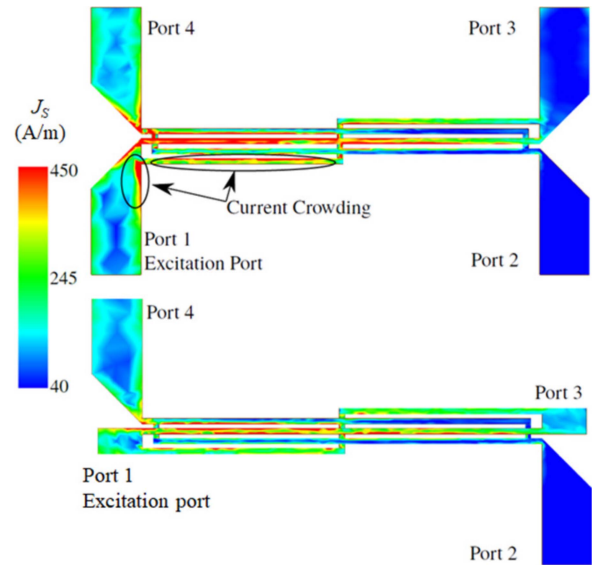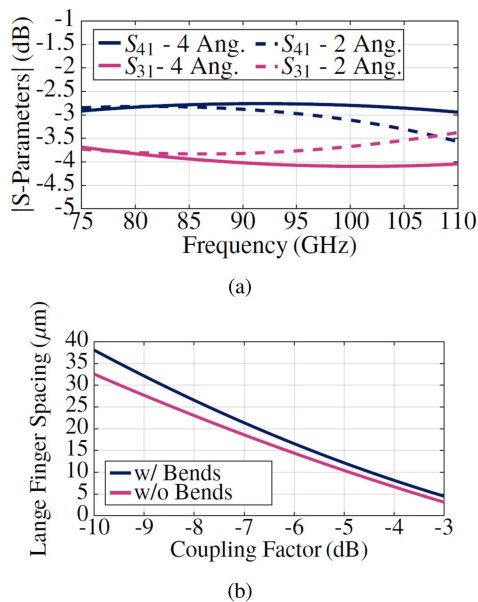
(a)

(b)

FIGURE 7. (a) Frequency shift for Lange coupler four- and two-bend manifolds, corresponding to Fig. 6. (b) The relationship between the coupling factor and finger spacing at 92.5 GHz for the two- and four-bend manifold Lange couplers.

right angle bend. In addition, the Lange coupler shifts in center operating frequency and errors associated with changed coupling factors across the serial splitter impact the overall performance of the PA. In Fig. 7, a design based on modeling using the traditional 4-angled bend Lange manifold shows amplitude variation of up to 5 dB at 110 GHz. Using EM modeling for a layout representative of how the Lange coupler is incorporated in the PA layout, the finger spacing as a function of coupling factor can be redesigned for improved wideband performance.

Stability is always a concern in PA design, particularly at W-band where 40 nm gate length HEMTs have high gains at lower frequencies. To insure stability of the design, multiple stability analysis methods are used during the design process including K factor and Nyquist stability criterion. Even- and odd-mode loop gain analysis helps ensure the stability of power combined stages [68], [69], [70].

The resulting even-mode loop gain simulations of the Unit PAs show a phase margin greater than 60°. Suppression of low-frequency gain is accomplished through accurate full-wave simulations of reactive matching networks, the addition of small resistors (about 5 Ω) in the dc gate paths, and on-chip capacitor ladder networks with increasing capacitor size from the RF path to the dc inputs. To eliminate odd-mode instabilities, resistors are placed on the symmetry lines before and after transistors in stages 2 and 3 and minimized in value using odd-mode loop-gain simulations.

B. MEASURED RESULTS
The balanced and serially-combined MMICs mounted on CuMo carriers and bonded to off-chip capacitors in the biasing
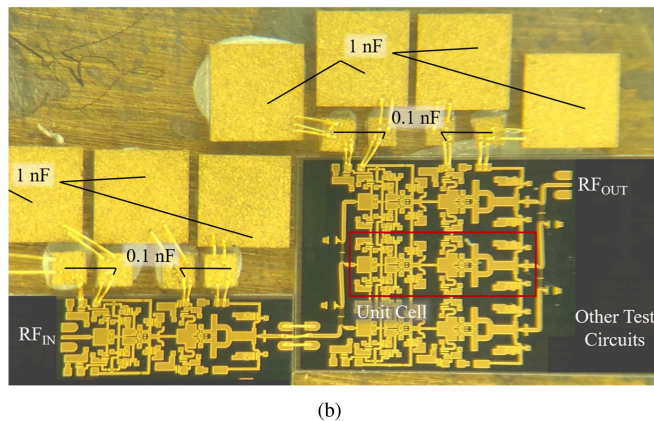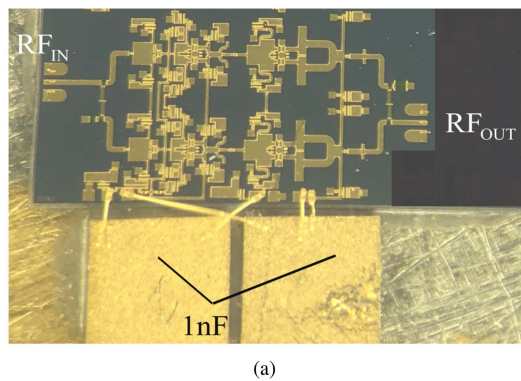

(a)

(b)

FIGURE 8. Photograph of the mounted (a) balanced and (b) serial MMIC PAs. The serial PA is bonded to an additional 3-stage "unit PA" driver which helps reach saturation in the lower part of W band.
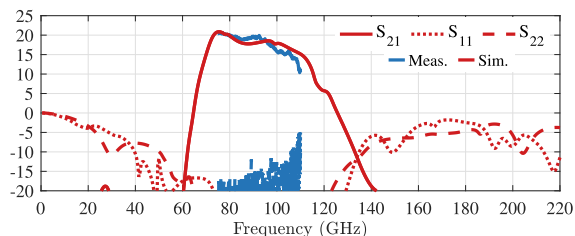

FIGURE 9. Simulated (red) and measured (blue) small-signal gain of the balanced PA MMIC [50].

network are shown in Fig. 8. Small-signal measurements show stable gain that correlates well with the model, showing peak gain of 20 dB at the lower end of the band decreasing to 15 dB at 100 GHz and 10 dB at 110 GHz, Fig. 9.

A power-calibrated scalar test setup is used for large-signal measurements. The CW W-band signal from a HP83650 A sweeper in Ka-band is followed by a Quinstar amplification chain (QPW-18402020-J0 Ka-band amplifier, QPM-93003 W passive tripler, QFL-B4SW00 low-pass filter and QPI-W01820-H4W02 W-band driver amplifier) with a maximum output power of roughly 18 dBm. An isolator with ~1.5 dB of forward transmission loss protects the amplification chain from any DUT mismatch. A 20-dB WiseWave coupler with a W-band power detector is calibrated with a
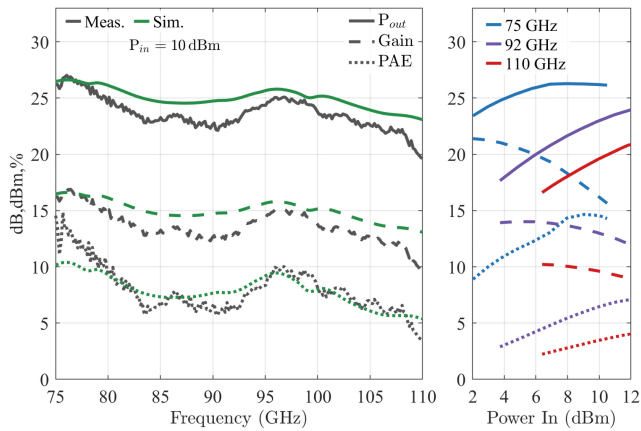
FIGURE 10. Measured (black) and simulated (green) large-signal performance of the balanced PA at $V_{DD} = +12$ V. over frequency (left) and as a function of input power at the lower, center and upper parts of W-band (right).

TABLE 5. Comparison of *V*- and *W*-Band GaN SPDT Switches

Freq (GHz)	Gate Length (nm)	IL (dB)	ISO (dB)	P$_{1dB}$ (dBm)	Year Ref.
60-110	40	0.9-1.4	>9	>24	2014 [53]$^{\triangle}$
80-100	40	1.3–1.7	>9	>24	2014 [53]
75-110	100	1.2–1.6	17.7–20	>25	2018 [31]
66-134	100	1.2–2.2	16.8–20	>25	2018 [31]
75-110	100	1.1–1.6	18.5–21.5	>25	2018 [31]
68-134	100	1.1–2.1	17.6–21.5	>25	2018 [31]
75-110	**40**	**0.9-3.5**	**25-30**	**>10^{+}**	**This Work$^{\triangle}$**
75-110	**40**	**1-2.2**	**15-20**	**>10^{+}**	**This Work$^{\triangle}$**
75-110	**40**	**1.8-8**	**30-40**	**>10^{+}**	**This Work$^{\blacksquare}$**

$^{\triangle}$ SPST, $^{\triangle}$ SPDT single FET, $^{\blacksquare}$ SPDT double FET
$^{+}$ Peak large-signal values @ P$_{IN}$ = 10 dBm and 76 GHz

W-band power meter. The results of these measurements are captured in Fig. 10 and show good agreement with simulations. The large signal gain at P$_{in}$ = 10 dBm is roughly 0.5–2 dB lower than simulated, but trends the same in frequency. The measured results, in Fig. 11, show 37.8% bandwidth from 75 to 110 GHz (where the gain is greater than 10 dB), a peak power of 25 dBm and a peak 1-dB compressed gain of 16 dB at 75 GHz.

In the measurement setup described above, the input power at the DUT is limited to 10 dBm. To obtain sufficient drive power for the serially combined PA, one of the 3-stage reactively-combined "unit" PAs is used as a driver, as shown in Fig. 8(b). The large-signal results for both the balanced and serially-combined PAs are included in Table 2.

IV. GAN MMIC SWITCHES
Microwave switches can be realized with the quarter-wave shunt topology. A source grounded HEMT is connected at its drain to a transmission line with electrical length of one quarter wavelength. The gate of the HEMT is then controlled to turn each path on or off. The *ON*-path is achieved by turning the device off, which acts as a grounded capacitor loading the line. At millimeter-wave frequencies, this off-state capacitance is typically resonated out with a shorted inductive stub placed directly at the drain node such that the impedance of the *ON* path is purely real and 50 Ω. The *OFF*-path is achieved by turning the device on, providing a short to the signal which appears as an open after the impedance transformation of the quarter-wave transmission line. The shorted stub at the drain node is in parallel with the source vias to decrease inductance and resistance to ground. This topology has been employed in GaN technologies in [31], [53] to realize W-band SPST and SPDT switches, summarized in Table 5.

For standard semiconductor technologies, high isolation scales with device periphery, resulting in a considerably large total gate width. Consequently, this increases the capacitance
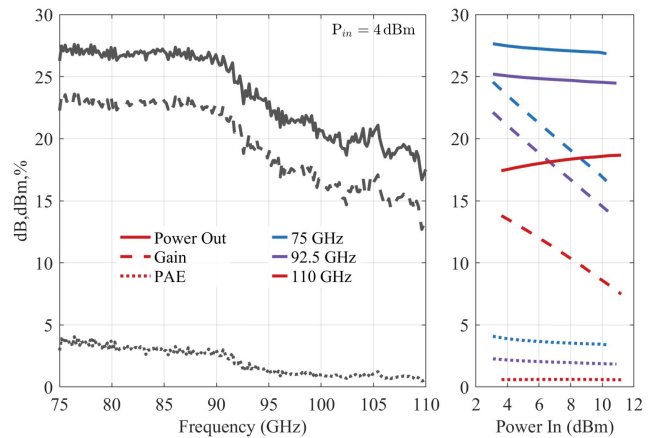

FIGURE 11. Measured large-signal performance of the serially-combined PA at 6 V drain bias with a 3-stage "unit PA" driver. Output power, gain and PAE over frequency (left) and over input power at the lower, center and upper parts of W-band (right).

C_{off} which, as previously described, is compensated by a parallel inductance or a shorted stub. This parallel resonant *LC* circuit and the electrical length of the $\lambda/4$ section are the main bandwidth limitation of a switch [31]. As with all millimeter-wave circuits, this topology must overcome the challenges of increased ohmic losses and parasitic reactance to maximize performance at W-band. Namely, terminating the quarter wave line with a perfect short cannot be easily implemented with just one HEMT. Two source-grounded HEMTs with gates tied have been demonstrated in InGaAs metamorphic HEMTs to increase isolation in the *OFF*-path, at the cost of insertion loss over millimeter wave frequencies [71].

We demonstrate this with switch designs in the HRL 40-nm T3 process, with a photo of the various switch layouts, among other components, shown in Fig. 12. A summary of measured results is shown in Fig. 13. The SPDT switch with a single shunted HEMT in Fig. 13(b) achieves an isolation between 15–20 dB and an insertion loss between 0.9–3 dB, while that in Fig. 13(c) achieves an isolation between 30–40 dB and an
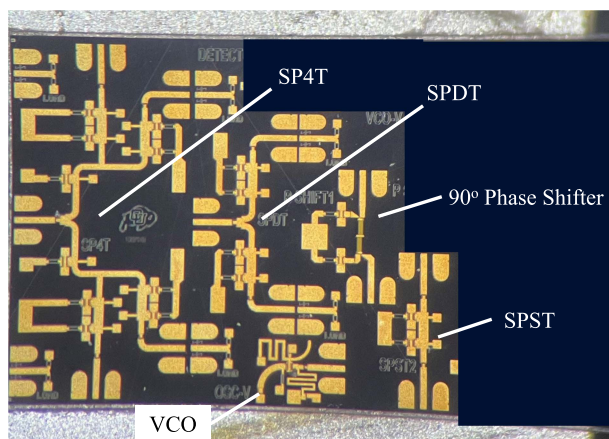
FIGURE 12. Photograph of MMIC reticle with RF switches, phase shifter, and *Ka*-band oscillator.
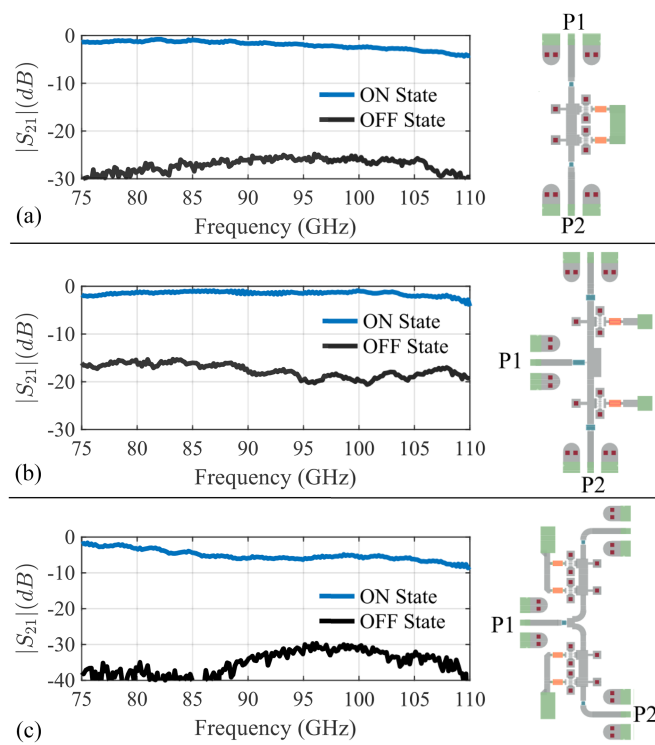

FIGURE 13. Measured small signal performance of three GaN switches implemented in the 40-nm HRL process: (a) SPST using double shunt HEMTs, (b) SPDT using single shunt HEMTs in each branch, and (c) SPDT using double shunt HEMTs in each branch.

insertion loss between 1.2–10 dB. The SP4T switch shown in the photo is currently being evaluated and any measured results will be included in the final version of the paper. To the authors' knowledge, this is the first such comparison of SPDT topologies for GaN devices over entire W-band.

V. PHASE SHIFTERS

Phase shifters are key components in RF front ends for phased arrays. Switched delay-line phase shifters are enabled by the
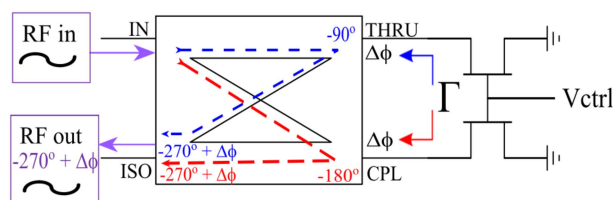

FIGURE 14. Circuit diagram of a reflective phase shifter. The variable reactances are implemented with varactor-connected HEMTs in the GaN MMIC implementation.

above described RF switches and the design is straightforward. However, the loss through the switches, number of dc controls, and large footprint make this design impractical for a circuit with many phase values at W-band. Vector modulators are also commonly synthesized to achieve phase shift, but cannot easily be implemented in GaN. Reflective phase shifters allow continuous tuning of phase through reflections from variable loads on two ports of a 90° hybrid coupler. Realizing tunable loads at W-band can be done by connecting HEMTs as varactors. Their small size and wide phase tuning range make them attractive for integrated front ends in GaN.

A 3 dB coupler splits the incoming signal power evenly between the "thru" and "coupled" ports, as displayed in Fig 14. $1/\sqrt{2}$ of the signal arrives at the "thru" port with a $-90°$ phase shift, while the remaining part at the coupled port is shifted by $-180°$. The varactors at the "thru" and "coupled" ports reflect the signal with a tunable phase shift corresponding to the varactor reactance, which is controlled through the gate bias voltage of the HEMT. The two signals then combine constructively at the isolated port with a $-270°$ shift added to the tunable phase. The reflected signals cancel at the input.

An analysis to optimize phase tuning is first performed in order to select the proper HEMT device size. The T3 GaN PDK offers transistors of four standard total peripheries: 50 μm, 150 μm, 300 μm, and 600 μm. Looking into the drain of these sourced-grounded devices, the largest tunable reactance range is found by sweeping the gate voltage from -1 V to $+1$ V. A 50 μm device is selected for the design, as it provides the greatest tunable reactance magnitude range of 51.4 Ω. The second key component of this design is a hybrid coupler. The Lange Coupler used for this design has less than 30 dB of return loss and at least 20 dB of isolation over an octave bandwidth from 60–120 GHz. The fabricated MMIC phase shifter is captured in the photograph of Fig. 12, and has an overall size of 1.05 mm by 0.75 mm.

The fabricated circuits, first presented in [72], are tested with a calibrated Rohde & Schwarz ZNA vector network analyzer, with ZVA-Z110E millimeter-wave converters for a full W-band characterization (75–110 GHz). Phase, return loss, and insertion loss are captured for each 5° increment in phase. The phase states are plotted in Fig. 15, displaying a tunable phase shift ranging from 90° to 105° over the entire bandwidth. $|S_{11}|$ and $|S_{21}|$ for each state are displayed in Fig. 16. Overall, the return loss ranges from 20 to 10 dB, indicating
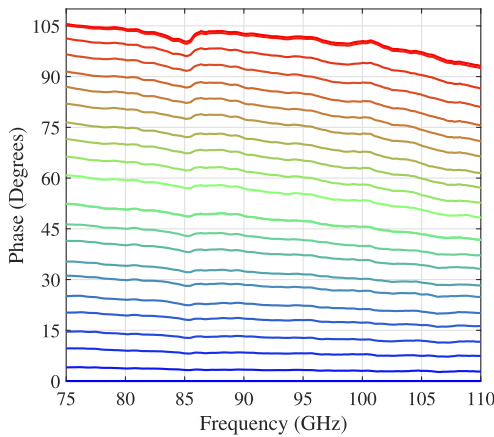
FIGURE 15. Measured phase states versus frequency across W band in 5° steps, for the gate control voltage from −1 V (blue) to +1 V (red).
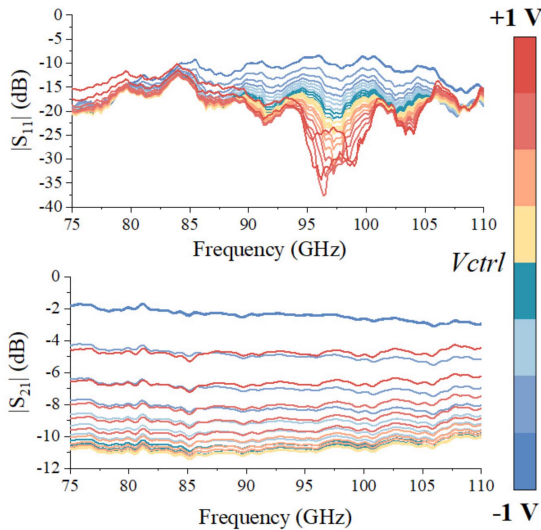

FIGURE 16. Measured $|S_{11}|$ (top) and $|S_{21}|$ (bottom) versus frequency as the control voltage is varied from −1 to +1 V.
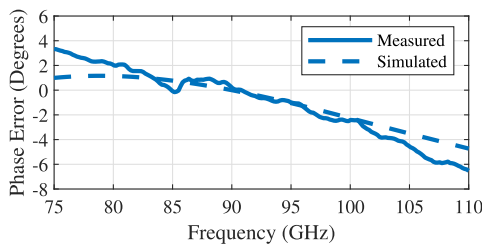

FIGURE 17. Measured (solid) and simulated (dashed) phase error vs frequency averaged over all states, relative to the phase at 90 GHz (center of the band).

that the device is well matched over the bandwidth. The insertion loss ranges from 2 to 11 dB across all of the phase states. Phase error is calculated across frequency relative to the phase at 90 GHz. The average measured and simulated phase errors are plotted in Fig. 17. Across the frequency band, the measured phase error is less than 10°, from −6° to +4°,
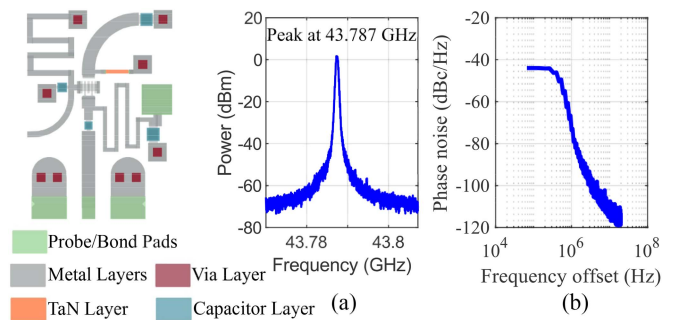

FIGURE 18. Fixed oscillator using a 4×37.5 μm HEMT at a 12 V drain bias. The gate of the device is shorted to ground through a resistor. Measured results using a HP8565E spectrum analyzer are shown: (a) power spectrum of the oscillator and (b) calculated associated phase noise.
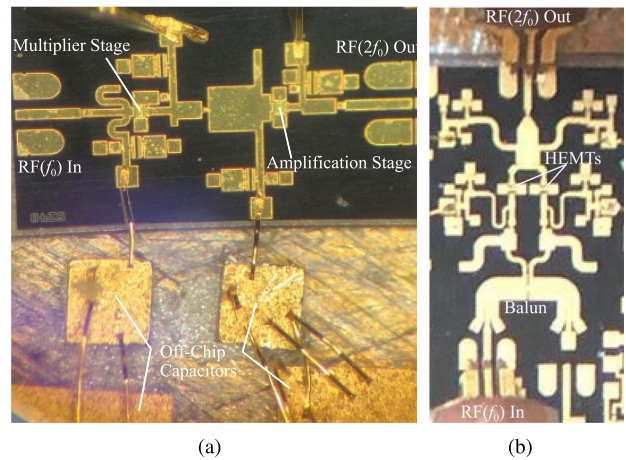

FIGURE 19. Photograph of the MMIC doublers for (a) single ended circuit with bond wires and off-chip capacitors and (b) balanced doubler circuit.

and is within 3° across the band, with the trend well predicted by simulations.

These results provide the greatest degree of phase shift for any GaN design over the entire W-band to the best of the authors' knowledge. Higher degrees of phase shift are realized by cascading multiple Lange sections with varactor tuners (phase shift bits). A similar GaN structure is provided in [53], but shifts a maximum of 45° for a one-bit structure and 67.5° for a two-bit structure over W-band. This design has the potential to operate over even wider bandwidths but is limited by the testing setup on hand. Finally, the amplitude error for each bit can be addressed by including a variable gain amplifier as in [73], before or after the phase shifter.

VI. FREQUENCY GENERATION AND TRANSLATION

Frequency generation for an integrated front end is briefly described next. An oscillator circuit at 44 GHz is shown with a measured spectrum in Fig. 18. Refering to the block diagram in Fig. 1, the LO at the fundamental is generated by frequency doubling the output of the oscillator. To accomplish that, a single-ended and balanced frequency doubler is implemented in the HRL T3 40 nm GaN process, shown in Fig. 19. Both
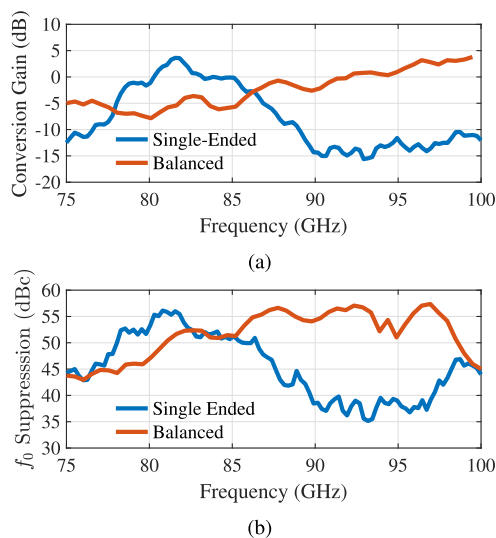
(a)

(b)

FIGURE 20. (a) Measured second harmonic output of both the single ended and balanced frequency doublers shown across the output frequency band at an input driver of 10 dBm. (b) Fundamental suppression for both the single-ended and balanced topology plotted over the output frequency spectrum at an input drive of 10 dBm.
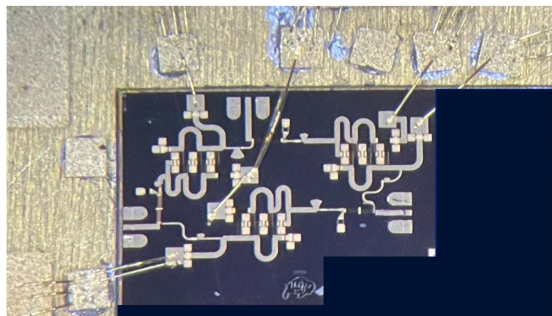

FIGURE 21. Photograph of W-Band active circulator MMIC currently under test.

doublers achieve conversion gain and over 10 dBm output power in the W-band frequency range. Reactive matching and cascading of a post-multiplication amplifier stage allows the single-ended topology to exhibit conversion gain and high fundamental suppression, Fig. 20. The single-ended topology outperforms the balanced topology in suppressing the fundamental. The post-amplifying HEMT along with the output matching network provide excellent fundamental suppression of over 35 dBc over the entire output band and over 50 dBc over 78 to 87 GHz.

Phase and amplitude imbalance of the planar Marchand balun as well as process variations degrade the suppression of the fundamental for the balanced topology, as described in more detail in [74]. To achieve the best conversion gain and fundamental suppression, a combination of both topologies is recommended. A doubling circuit arranged in a balanced configuration with post-multiplication amplifier benefits from the power-combining providing increased output power and
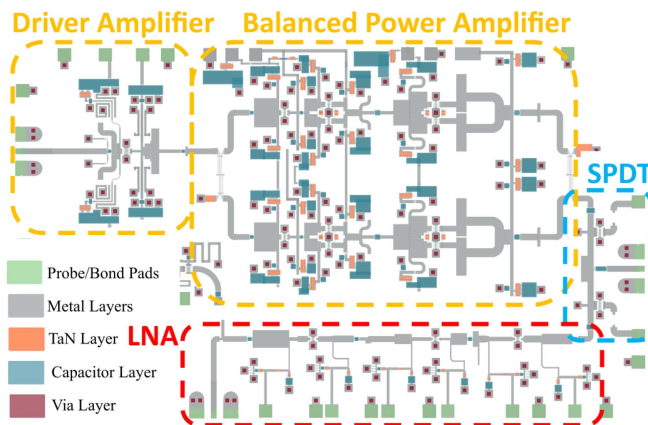

FIGURE 22. Layout of W-band front end integrated MMIC. The TX mode consists of a pre-amplifier driving a balanced power amplifier which connects to the output antenna port through a SPDT switch. For the RX mode, the SPDT output is the input port which is then directly connected to a 3-stage LNA.
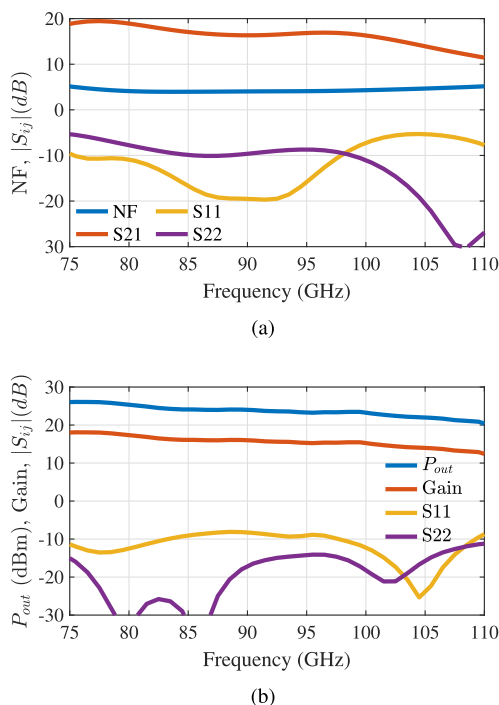

(a)

(b)

FIGURE 23. Simulated results of the front end in Fig. 22: (a) noise factor and S parameters in RX mode and (b) the output power, power gain and input/output match in TX mode.

the post-amplification providing additional second harmonic power and fundamental suppression.

VII. CONCLUSION
This work presents a review of GaN MMICs from 50–110 GHz published to date, and new MMICs in the HRL 40-nm process designed towards an integrated front end. For a half-duplex case, the next step in integration is the combination of the balanced PA with a driver in the transmit path, followed by a low insertion loss SPDT switch and 3-stage

LNA in the receive path. The layout of this chip which is currently being fabricated is shown in Fig. 22, with simulated performance shown in Fig. 23. For a full-duplex front end, future work includes scaling the X-band active circulator in [61] to operate at W-band. This design provides gain in the through path and sufficiently isolates the reverse paths. Linearity and noise must also meet stringent requirements to maintain the integrity of the signals. A fabricated circuit currently under characterization is displayed in Fig. 21.

As GaN technology continues to improve, higher levels of integration are becoming possible. Packaging techniques with thermal management are necessary to make W-band front ends practical. Several different levels of package level integration have already been explored [75], [76]. A comparison between water cooling and air cooling was done for a 37 W power amplifier module [51]. Results indicate a viable solid-state integrated approach for V- and W-band front ends.

REFERENCES

[1] C. Riva, C. Capsoni, L. Luini, M. Luccini, R. Nebuloni, and A. Martellucci, "The challenge of using the W band in satellite communication," *Int. J. Satell. Commun. Netw.*, vol. 32, no. 3, pp. 187–200, 2014.

[2] H. J. Liebe, T. Manabe, and G. A. Hufford, "Millimeter-wave attenuation and delay rates due to fog/cloud conditions," *IEEE Trans. Antennas Propag.*, vol. 37, no. 12, pp. 1617–1612, Dec. 1989.

[3] S. Sun, T. S. Rappaport, M. Shafi, P. Tang, J. Zhang, and P. J. Smith, "Propagation models and performance evaluation for 5G millimeter-wave bands," *IEEE Trans. Veh. Technol.*, vol. 67, no. 9, pp. 8422–8439, Sep. 2018.

[4] P. M. Asbeck, N. Rostomyan, M. özen, B. Rabet, and J. A. Jayamon, "Power amplifiers for mm-wave 5G applications: Technology comparisons and CMOS-SOI demonstration circuits," *IEEE Trans. Microw. Theory Techn.*, vol. 67, no. 7, pp. 3099–3109, Jul. 2019.

[5] K. Brown et al., "Ultra-compact high speed MMW transceiver using GaN power amplifier technology," in *Proc. IEEE MTT-S Int. Microw. Symp.*, 2015, pp. 1–3.

[6] F. Boes et al., "Multi-gigabit E-band wireless data transmission," in *Proc. IEEE MTT-S Int. Microw. Symp.*, 2015, pp. 1–4.

[7] O. Kodheli et al., "Satellite communications in the new space era: A survey and future challenges," *IEEE Commun. Surveys Tuts.*, vol. 23, no. 1, pp. 70–109, Jan.–Mar. 2021.

[8] D. Bleh et al., "A 100GHz FMCW MIMO radar system for 3D image reconstruction," in *Proc. Eur. Radar Conf.*, 2016, pp. 37–40.

[9] C. Rhoads and D. S. Goshi, "A scalable W-band imaging radar development platform," in *Proc. IEEE Radar Cnf.*, 2018, pp. 0344–0348.

[10] H. Cheng, S. Li, H. Zheng, H. Jing, and H. Sun, "A W-band auto-focus holographic imaging system for security screening," *IEICE Electron. Exp.*, vol. 14, no. 11, 2017, Art. no. 20170347.

[11] I. Nasr et al., "A highly integrated 60GHz 6-channel transceiver with antenna in package for smart sensing and short-range communications," *IEEE J. Solid-State Circuits*, vol. 51, no. 9, pp. 2066–2076, Sep. 2016.

[12] A. Arbabian, S. Callender, S. Kang, M. Rangwala, and A. M. Niknejad, "A 94 GHz mm-wave-to-baseband pulsed-radar transceiver with applications in imaging and gesture recognition," *IEEE J. Solid-State Circuits*, vol. 48, no. 4, pp. 1055–1071, Apr. 2013.

[13] D. Bleh et al., "W-band time-domain multiplexing FMCW MIMO radar for far-field 3-D imaging," *IEEE Trans. Microw. Theory Techn.*, vol. 65, no. 9, pp. 3474–3484, Sep. 2017.

[14] S.-Y. Jeon et al., "W-band MIMO FMCW radar system with simultaneous transmission of orthogonal waveforms for high-resolution imaging," *IEEE Trans. Microw. Theory Techn.*, vol. 66, no. 11, pp. 5051–5064, Nov. 2018.

[15] U. Alkus, A. B. Sahin, and H. Altan, "Stand-off through-the-wall w-band millimeter-wave imaging using compressive sensing," *IEEE Geosci. Remote Sens. Lett.*, vol. 15, no. 7, pp. 1025–1029, Jul. 2018.

[16] R. H. Geschke, O. Arpe, R. Brauns, and C. Krebs, "Enhanced hidden object detection with a circularly polarized W-band imaging radar system," in *Proc. 15th Eur. Radar Conf.*, 2018, pp. 237–240.

[17] F. Nsengiyumva, C. Migliaccio, L. Brochier, J.-Y. Dauvignac, I. Aliferis, and C. Pichot, "New *W*-band scattering measurement system: Proof of concept and results for 2-D objects," *IEEE Trans. Antennas Propag.*, vol. 66, no. 12, pp. 7224–7236, Dec. 2018.

[18] M. Kishida, K. Ohguchi, and M. Shono, "79 GHz-band high-resolution millimeter-wave radar," *Fujitsu. Sci. Tech. J.*, vol. 51, no. 4, pp. 55–59, 2015.

[19] R. A. Alhalabi and G. M. Rebeiz, "A 77-81-GHz 16-element phased-array receiver with 50 beam scanning for advanced automotive radars," *IEEE Trans. Microw. Theory Techn.*, vol. 62, no. 11, pp. 2823–2832, Nov. 2014.

[20] T.-Y. Lee, V. Skvortsov, M.-S. Kim, S.-H. Han, and M.-H. Ka, "Application of *W*-band FMCW radar for road curvature estimation in poor visibility conditions," *IEEE Sensors J.*, vol. 18, no. 13, pp. 5300–5312, Jul. 2018.

[21] A. Hati and C. W. Nelson, "*W*-band vibrometer for noncontact thermoacoustic imaging," *IEEE Trans. Ultrason., Ferroelect., Freq. Control*, vol. 66, no. 9, pp. 1536–1539, Sep. 2019.

[22] H. Kim and J. Jeong, "Non-contact measurement of human respiration and heartbeat using W-band Doppler radar sensor," *Sensors*, vol. 20, no. 18, 2020, Art. no. 5209.

[23] Z. D. Taylor et al., "THz medical imaging: In vivo hydration sensing," *IEEE Trans. THz Sci. Technol.*, vol. 1, no. 1, pp. 201–219, Sep. 2011.

[24] R. Wang, C. Hu, X. Fu, T. Long, and T. Zeng, "Micro-Doppler measurement of insect wing-beat frequencies with W-band coherent radar," *Sci. Rep.*, vol. 7, no. 1, pp. 1–8, 2017.

[25] E. D. Cohen, "The MIMIC program–A retrospective," *IEEE Microw. Mag.*, vol. 13, no. 4, pp. 77–88, May/Jun. 2012.

[26] J. J. Sowers et al., "A 36 w, v-band, solid state source," in *IEEE MTT-S Int. Microw. Symp. Dig.*, 1999, pp. 235–238.

[27] K. Shinohara et al., "Scaling of GaN HEMTs and Schottky diodes for submillimeter-wave MMIC applications," *IEEE Trans. Electron Devices*, vol. 60, no. 10, pp. 2982–2996, Oct. 2013.

[28] M. Božanić and S. Sinha, "Emerging transistor technologies capable of terahertz amplification: A way to re-engineer terahertz radar sensors," *Sensors*, vol. 19, no. 11, 2019, Art. no. 2454.

[29] S. S. M. Roberg and S. Chen, "Qorvo millimeter wave GaN MMIC processes, circuits & integration technology," in *Proc. Eur. Microw. Week, Vol. Workshop mm-Wave GaN MMICs*, 2022.

[30] D. Denninghoff, "High-efficiency GaN MMIC technologies for w-band applications and beyond," in *Proc. Eur. Microw. Week, Vol. Workshop mm-Wave GaN MMICs*, 2022.

[31] F. Thome, E. Ture, P. Brückner, R. Quay, and O. Ambacher, "W-band SPDT switches in planar and tri-gate 100-nm gate-length GaN-HEMT technology," in *Proc. 11th German Microw. Conf.*, 2018, pp. 331–334.

[32] M. Rocchi, "100,60 and 40 nm GaN/Si power amplifiers to complement Si solutions for 5G and 6G applications," in *Proc. Eur. Microw. Week, Vol. Workshop mm-Wave GaN MMICs*, 2022.

[33] D. S. R. Q. F. Thome and P. Neininger, "Broadband operation of GaN mm-wave MMICs," in *Proc. Eur. Microw. Week, Vol. Workshop mm-Wave GaN MMICs*, 2022.

[34] K. Felch et al., "Operating experience on six 110 GHz, 1 MW gyrotrons for ECH applications," *Nucl. Fusion*, vol. 48, no. 5, 2008, Art. no. 054008.

[35] K. Brown et al., "7 kW GaN W-band transmitter," in *Proc. IEEE MTT-S Int. Microw. Symp.*, 2016, pp. 1–3.

[36] A. Brown et al., "High power, high efficiency E-band GaN amplifier MMICs," in *Proc. IEEE Int. Conf. Wireless Inf. Technol. Syst.*, 2012, pp. 1–4.

[37] D. Schwantuschke, B. J. Godejohann, P. Brückner, A. Tessmann, and R. Quay, "mm-wave operation of AlN/GaN-devices and MMICs at V- & W-band," in *Proc. 22nd Int. Microw. Radar Conf.*, 2018, pp. 238–241.

[38] M. Micovic et al., "W-band GaN MMIC with 842 mW output power at 88 GHz," in *Proc. IEEE MTT-S Int. Microw. Symp.*, 2010, pp. 237–239.

[39] A. Brown, K. Brown, J. Chen, K. C. Hwang, N. Kolias, and R. Scott, "W-band GaN power amplifier MMICs," in *Proc. IEEE MTT-S Int. Microw. Symp.*, 2011, pp. 1–4.

[40] Y. Niida et al., "3.6 W/mm high power density W-band InAlGaN/GaN HEMT MMIC power amplifier," in *Proc. IEEE Topical Conf. Power Amplifiers Wireless Radio Appl.*, 2016, pp. 24–26.

[41] E. Ture et al., "First demonstration of W-band tri-gate GaN-HEMT power amplifier MMIC with 30 dBm output power," in *Proc. IEEE MTT-S Int. Microw. Symp.*, 2017, pp. 35–37.

[42] W. Shaobing et al., "W-band AlGaN/GaN MMIC pa with 3.1 W output power," in *Proc. 14th China Int. Forum Solid State Lighting: Int. Forum Wide Bandgap Semicond. China*, 2017, pp. 219–223.

[43] W. Wang, F. Guo, T. Chen, and K. Wang, "24.8 a W-band power amplifier with distributed common-source GaN HEMT and 4-way Wilkinson-lange combiner achieving 6 W output power and 18% PAE at 95 GHz," in *Proc. IEEE Int. Solid- State Circuits Conf.*, 2020, pp. 376–378.

[44] P. E. Longhi, S. Colangeli, W. Ciccognani, L. Pace, R. Leblanc, and E. Limiti, "C to V-band cascode distributed amplifier design leveraging a double gate length gallium nitride on silicon process," in *Proc. IEEE/MTT-S Int. Microw. Symp.*, 2020, pp. 409–412.

[45] A. Margomenos et al., "70–105 GHz wideband GaN power amplifiers," in *Proc. 7th Eur. Microw. Integr. Circuit Conf.*, 2012, pp. 199–202.

[46] J. Schellenberg, B. Kim, and T. Phan, "W-band, broadband 2 W MMIC GaN," in *IEEE MTT-S Int. Microw. Symp. Dig.*, 2013, pp. 1–4.

[47] J. Schellenberg, A. Tran, L. Bui, A. Cuevas, and E. Watkins, "37 W, 75–100 GHz GaN power amplifier," in *Proc. IEEE MTT-S Int. Microw. Symp.*, 2016, pp. 1–4.

[48] M. Cwiklinski et al., "Full W-band GaN power amplifier MMICs using a novel type of broadband radial stub," *IEEE Trans. Microw. Theory Techn.*, vol. 66, no. 12, pp. 5664–5675, Dec. 2018.

[49] Q. Ge, H. Tao, W. Wang, D. Shang, and R. Liu, "A 24.2 dBm full W band GaN power amplifier with about 40 GHz of bandwidth," in *Proc. IEEE MTT-S Int. Wireless Symp.*, 2021, pp. 1–3.

[50] S. Verploegh, T. Sonnenberg, M. Pinto, A. Babenko, and Z. Popović, "On-chip power combining with 3-stage 75–110 GHz GaN MMIC power amplifiers," in *Proc. 51st Eur. Microw. Conf.*, 2022, pp. 890–893.

[51] J. Schellenberg, A. Tran, L. Bui, A. Cuevas, and E. Watkins, "37 W, 75–100 GHz GaN power amplifier," in *Proc. IEEE MTT-S Int. Microw. Symp.*, 2016, pp. 1–4.

[52] J. M. Schellenberg, "A 2-W W-band GaN traveling-wave amplifier with 25-GHz bandwidth," *IEEE Trans. Microw. Theory Techn.*, vol. 63, no. 9, pp. 2833–2840, Sep. 2015.

[53] A. Margomenos et al., "W-band GaN receiver components utilizing highly scaled, next generation GaN device technology," in *Proc. IEEE Compound Semicond. Integr. Circuit Symp.*, 2014, pp. 1–4.

[54] A. Kurdoghlian et al., "First demonstration of broadband W-band and D-band GaN MMICs for next generation communication systems," in *Proc. IEEE MTT-S Int. Microw. Symp.*, 2017, pp. 1126–1128.

[55] F. Thome, P. Brückner, S. Leone, and R. Quay, "A wideband E/W-band low-noise amplifier MMIC in a 70-nm gate-length GaN HEMT technology," *IEEE Trans. Microw. Theory Techn.*, vol. 70, no. 2, pp. 1367–1376, Feb. 2022.

[56] K. W. Kobayashi and V. Kumar, "A broadband 70&-110-GHz E-/W-band LNA using a 90-nm T-gate GaN HEMT technology," *IEEE Microw. Wireless Compon. Lett.*, vol. 31, no. 7, pp. 885–888, Jul. 2021.

[57] S. Lardizabal, K. C. Hwang, J. Kotce, A. Brown, and A. Fung, "Wideband W-band GAN LNA MMIC with state-of-the-art noise figure," in *Proc. IEEE Compound Semicond. Integr. Circuit Symp.*, 2016, pp. 1–4.

[58] I. Kallfass et al., "A highly linear 84 GHz low noise amplifier MMIC in AlGaN/GaN HEMT technology," in *Proc. IEEE MTT-S Int. Microw. Workshop Ser. Millimeter Wave Integration Technol.*, 2011, pp. 144–147.

[59] R. Weber et al., "A beyond 110 GHz GaN cascode low-noise amplifier with 20.3 dBm output power," in *Proc. IEEE/MTT-S Int. Microw. Symp.*, 2018, pp. 1499–1502.

[60] X. Tong, P. Zheng, and L. Zhang, "Low-noise amplifiers using 100-nm gate length GaN-on-silicon process in W-band," *IEEE Microw. Wireless Compon. Lett.*, vol. 30, no. 10, pp. 957–960, Oct. 2020.

[61] L. Marzall, S. Verploegh, T. Cappello, M. Roberg, and Z. Popović, "Active MMIC circulator performance in a phased-array-like environment," in *Proc. 50th Eur. Microw. Conf.*, 2021, pp. 1186–1189.

[62] X. Lan et al., "A V-Band monolithic AlGaN/GaN VCO," *IEEE Microw. Wireless Compon. Lett.*, vol. 18, no. 6, pp. 407–409, Jun. 2008.

[63] R. Weber et al., "A 67 GHz GaN voltage-controlled oscillator MMIC with high output power," *IEEE Microw. Wireless Compon. Lett.*, vol. 23, no. 7, pp. 374–376, Jul. 2013.

[64] Y. Nakasha et al., "E-band 85-mW oscillator and 1.3-W amplifier ICs using 0.12μm GaN HEMTs for millimeter-wave transceivers," in *Proc. IEEE Compound Semicond. Integr. Circuit Symp.*, 2010, pp. 1–4.

[65] T. N. Thi Do, Y. Yan, and D. Kuylenstierna, "A low phase noise W-band MMIC GaN HEMT oscillator," in *Proc. IEEE Asia-Pacific Microw. Conf.*, 2020, pp. 113–115.

[66] R. Weber, D. Schwantuschke, P. Brückner, R. Quay, F. van Raay, and O. Ambacher, "A 92 GHz GaN HEMT voltage-controlled oscillator MMIC," in *Proc. IEEE MTT-S Int. Microw. Symp.*, 2014, pp. 1–4.

[67] D. Kim and S. Jeon, "W- and G-band GaN voltage-controlled oscillators with high output power and high efficiency," *IEEE Trans. Microw. Theory Techn.*, vol. 69, no. 8, pp. 3908–3916, Aug. 2021.

[68] C. Campbell, *Microwave Monolithic Power Amplifier Design*. Atlanta, GA, USA: American Cancer Society, 2013.

[69] A. Suarez, "Check the stability: Stability analysis methods for microwave circuits," *IEEE Microw. Mag.*, vol. 16, no. 5, pp. 69–90, Jun. 2015.

[70] M. Pinto, "Millimeter-wave GaN solid-state arrays," Ph.D. dissertation, Dept. Elect. Comp. and Energy Eng., University of Colorado, Boulder, CO, USA, 2019.

[71] I. Kallfass, S. Diebold, H. Massler, S. Koch, M. Seelmann-Eggebert, and A. Leuther, "Multiple-throw millimeter-wave FET switches for frequencies from 60 up to 120 GHz," in *Proc. 38th Eur. Microw. Conf.*, 2008, pp. 1453–1456.

[72] A. Romano, T. Sonnenberg, S. Verploegh, T. Barton, and Z. Popovic, "A W-band GaN MMIC continuous 90° reflective phase shifter," in *Proc. IEEE 22nd Annu. Wireless Microw. Technol. Conf.*, 2022, pp. 1–4.

[73] S. Diebold et al., "AlGaN/GaN-based variable gain amplifiers for W-band operation," in *IEEE MTT-S Int. Microw. Symp. Dig.*, 2013, pp. 1–4.

[74] T. Sonnenberg, M. Pinto, S. Verploegh, and Z. Popović, "W-band GaN frequency multipliers," *IEEE Trans. Microw. Theory Techn.*, 2022.

[75] J. Soric et al., "A 100-W W-band GaN SSPA," *IEEE Microw. Wireless Compon. Lett.*, vol. 32, no. 6, pp. 712–715, Jun. 2022.

[76] J. Schellnberg, "Millimeter-wave GaN SSPAs: Technology to power 5G and the future," in *Proc. IEEE BiCMOS Compound Semicond. Integr. Circuits Technol. Symp.*, 2020, pp. 1–7.

TIMOTHY SONNENBERG (Student Member, IEEE) received the B.Sc. degree from the North Carolina State University, Raleigh, NC, USA, in 2014. He is currently working toward the Ph.D. degree with the University of Colorado, Boulder, CO, USA. During his senior year and after graduation, he was with Wolfspeed, a CREE company, assisting the RF Device and Process Development team with testing and design in several different GaN processes. His main research interests include mmWave MMIC design in Gallium Nitride (GaN) for various types of circuits including but not limited to power amplifiers, frequency multipliers, mixers, and passive components and oscillators.

ANTHONY ROMANO (Student Member, IEEE) received the B.S. degree in electrical engineering from Drexel University, Philadelphia, PA, USA, in 2017, and the M.S. degree in electrical engineering from Northeastern University, Boston, MA, USA, in 2020. Before returning to Graduate School with Northeastern, he was a MMIC/RFIC Designer with Northrop Grumman Corporation. In Fall 2020, he joined CU Boulder to pursue his Ph.D. with a research focus on MMIC design. He is currently working on several millimeter-wave projects at Ka-V- and W-Band.

SHANE VERPLOEGH (Member, IEEE) received the Ph.D. degree in applied electromagnetics from the University of Colorado Boulder, Boulder, CO, USA. He is currently a Senior RF Engineer with ColdQuanta who specializes in quantum sensing and communications using rydberg atoms. He researched high-power transmit architectures in the V- and W-bands with specific focus towards power amplifier design and characterization in experimental T-gate GaN processes and novel 3D printing packaging techniques using direct metal laser sintering with the University of Colorado.

MAURICIO PINTO (Member, IEEE) received the Ph.D. degree in electrical engineering from the University of Colorado at Boulder, Boulder, CO, USA, in 2019. From 2010 to 2014, he was with the Weapons Division, Naval Air Warfare Center, China Lake, CA, USA, where he was involved in RF front ends for airborne and landbased defense systems. From 2019 to 2021, he was with Raytheon Technologies, El Segundo, CA, USA, as a Principal Electrical Engineer working on T/R modules for phased array radar systems. In 2021, he joined the Infrastructure and Defense Products Business Unit, Qorvo, Inc., Richardson, TX, USA, where he is currently a Senior MMIC Design Engineer working on gallium-nitride MMIC products. Dr. Pinto was the recipient of the Branko Popovic Graduate Fellowship of applied electromagnetics at the College of Engineering and Applied Sciences, University of Colorado Boulder, in May 2018.

ZOYA POPOVIĆ (Fellow, IEEE) received the Dipl.Ing. degree from the University of Belgrade, Belgrade, Serbia, and the Ph.D. degree from Caltech, Pasadena, CA, USA. She is currently a Distinguished Professor and the Lockheed Martin Endowed Chair of Electrical Engineering with the University of Colorado, Boulder, CO, USA. She has graduated more than 55 Ph.D. students and currently advises 15 graduate students in various areas of high-frequency electronics and microwave engineering. She was the recipient of two IEEE MTT Microwave Prizes for best journal papers, White House NSF Presidential Faculty Fellow award, URSI Issac Koga Gold Medal, ASEE/HP Terman Medal, and German Humboldt Research Award. She was named an IEEE MTT Distinguished Educator, in 2013, and a Distinguished Research Lecturer with the University of Colorado, in 2016. She has a husband physicist and three daughters who can all solder.